Angular Distribution Models for Top-of-Atmosphere Radiative Flux Estimation from the Clouds and the Earth's Radiant Energy System Instrument on the *Terra* Satellite. Part I: Methodology

NORMAN G. LOEB AND SEIJI KATO

Center for Atmospheric Sciences, Hampton University, Hampton, Virginia

KONSTANTIN LOUKACHINE

Science Applications International Corporation, Hampton, Virginia

NATIVIDAD MANALO-SMITH

Analytical Services and Materials, Hampton, Virginia

(Manuscript received 26 May 2004, in final form 10 September 2004)

ABSTRACT

The Clouds and Earth's Radiant Energy System (CERES) provides coincident global cloud and aerosol properties together with reflected solar, emitted terrestrial longwave, and infrared window radiative fluxes. These data are needed to improve the understanding and modeling of the interaction between clouds, aerosols, and radiation at the top of the atmosphere, surface, and within the atmosphere. This paper describes the approach used to estimate top-of-atmosphere (TOA) radiative fluxes from instantaneous CERES radiance measurements on the *Terra* satellite. A key component involves the development of empirical angular distribution models (ADMs) that account for the angular dependence of the earth's radiation field at the TOA. The CERES *Terra* ADMs are developed using 24 months of CERES radiances, coincident cloud and aerosol retrievals from the Moderate Resolution Imaging Spectroradiometer (MODIS), and meteorological parameters from the Global Modeling and Assimilation Office (GMAO)'s Goddard Earth Observing System (GEOS) Data Assimilation System (DAS) V4.0.3 product. Scene information for the ADMs is from MODIS retrievals and GEOS DAS V4.0.3 properties over the ocean, land, desert, and snow for both clear and cloudy conditions. Because the CERES *Terra* ADMs are global, and far more CERES data are available on *Terra* than were available from CERES on the *Tropical Rainfall Measuring Mission* (*TRMM*), the methodology used to define CERES *Terra* ADMs is different in many respects from that used to develop CERES *TRMM* ADMs, particularly over snow/sea ice, under cloudy conditions, and for clear scenes over land and desert.

1. Introduction

One of the largest uncertainties in global climate models is the representation of how clouds and aerosols influence the earth's radiation budget (ERB) at the surface, within the atmosphere, and at the top of the atmosphere. Because of the uncertainty in cloud–aerosol–radiation interactions, model predictions of climate change vary widely from one model to the next (Cess et al. 1990, 1996; Cubasch et al. 2001). To improve our understanding of cloud–aerosol–radiation interactions, and to identify key areas where climate models can be improved, global observations are needed. The central objective of the Clouds and the Earth's Radiant Energy System (CERES) mission is to provide accurate global cloud, aerosol, and radiation data products to facilitate research addressing the role clouds and aerosols play in modulating the radiative energy flow within the earth–atmosphere system (Wielicki et al. 1996). The two CERES satellite instruments aboard the *Terra* spacecraft provide highly accurate shortwave (SW), longwave (LW), and infrared window (WN) radiance measurements and top-of-atmosphere (TOA) radiative flux estimates globally at a 20-km spatial resolution. These data, together with coincident cloud and aerosol properties inferred from the Moderate Resolution Imaging Spectroradiometer (MODIS), provide a consistent cloud–aerosol–radiation dataset for studying clouds and aerosols, and their influence on the ERB.

One of the challenges involved in producing ERB

Corresponding author address: Dr. Norman G. Loeb, Mail Stop 420, NASA Langley Research Center, Hampton, VA 23681-2199. E-mail: n.g.loeb@larc.nasa.gov

datasets from satellites is the need to convert the radiance measurements at a given sun–Earth–satellite configuration to outgoing reflected solar and emitted thermal TOA radiative fluxes. To estimate TOA fluxes from measured CERES radiances, one must account for the angular dependence in the radiance field, which is a strong function of the physical and optical characteristics of the scene (e.g., surface type, cloud fraction, cloud/aerosol optical depth, cloud phase, etc.), as well as the illumination angle. Because the CERES instrument can rotate in azimuth as it scans in elevation, it acquires data over a wide range of angles. Consequently, one can construct angular distribution models (ADMs) for radiance-to-flux conversion directly from the CERES measurements. Furthermore, because CERES and MODIS are on the same spacecraft, the ADMs can be derived as a function of MODIS-based scene-type parameters that have a strong influence on radiance anisotropy.

The first set of CERES ADMs were developed using 9 months of CERES and Visible Infrared Scanner (VIRS) data from the *Tropical Rainfall Measuring Mission* (*TRMM*) satellite between 38°S and 38°N from January to August 1998 and March 2000 (Loeb et al. 2003a). Because *TRMM* is in a 350-km circular precessing orbit with a 35° inclination angle, CERES *TRMM* sampled the full range of solar zenith angles over a region every 46 days. Unfortunately, the CERES *TRMM* instrument suffered a voltage-converter anomaly and acquired only 9 months of scientific data. In contrast, the CERES instruments on *Terra* have, thus far, acquired over 4 yr of global data with coarser spatial resolution (20 km versus 10 km for CERES *TRMM*) from a sun-synchronous orbit at an altitude of 705 km. Because of the differences in spatial resolution and geographical coverage between the CERES instruments on *TRMM* and *Terra*, direct application of the CERES *TRMM* ADMs to CERES *Terra* data is inappropriate, particularly at midlatitudes and in the polar regions.

The increased sampling that is available from CERES *Terra* provides a unique opportunity to develop a more comprehensive set of ADMs that are suitable for radiance-to-flux conversion with CERES *Terra* data and data from other broadband instruments with similar characteristics and orbital geometry. This paper is the first in a two-part series. Part I describes the development of new CERES *Terra* SW, LW, and WN ADMs from 2 yr of global data. Where appropriate, we compare the methodology used to produce CERES *Terra* ADMs with that used in Loeb et al. (2003a) to produce CERES *TRMM* ADMs. Part II will present extensive validation results in order to assess the accuracy of SW, LW, and WN TOA fluxes that are derived from the CERES *Terra* ADMs. TOA fluxes from the new *Terra* ADMs will also be compared with those from *TRMM* ADMs, as well as with fluxes based on algorithms developed during the Earth Radiation Budget Experiment (ERBE) (Smith et al. 1986; Suttles et al. 1992).

2. Observations

The *Terra* spacecraft, launched on 18 December 1999, carries two identical CERES instruments: Flight Model (FM)-1 and -2. *Terra* is in a descending sun-synchronous orbit with an equator-crossing time of 1030 LST. The CERES instrument is a scanning broadband radiometer that measures filtered radiances in the SW (wavelengths between 0.3 and 5 μm), total (TOT; wavelengths between 0.3 and 200 μm), and WN (wavelengths between 8 and 12 μm) regions. To correct for the imperfect spectral response of the instrument, the filtered radiances are converted to unfiltered reflected solar, unfiltered emitted terrestrial LW and WN radiances (Loeb et al. 2001). On *Terra*, CERES has a spatial resolution of approximately 20 km (equivalent diameter). One of the unique features of CERES is its ability to scan in either a fixed, rotating or programmable azimuth plane scan mode. Operationally, one CERES instrument is placed in a cross-track scan mode to optimize spatial sampling for time–space averaging (Young et al. 1998), while the second instrument is either in a rotating azimuth plane (RAP), an along-track, or a programmable azimuth plane (PAP) scan mode. In the RAP mode, the instrument scans in elevation as it rotates in azimuth thus acquiring radiance measurements from a wide range of viewing configurations. In PAP mode, CERES is programmed to collect measurements for a specific field campaign, for intercalibration with other instruments (e.g., CERES on *TRMM*, the Geostationary Earth Radiation Budget Instrument), or to augment sampling in specific viewing geometries (e.g., the principal plane). The nominal schedule is to operate the second CERES instrument in along-track mode every 15 days and in RAP mode the remainder of the time. In contrast, CERES *TRMM* was in RAP mode only every third day, and in along-track mode every 15 days. The increase in RAP sampling for CERES *Terra*, together with its relatively small range of solar zenith angle coverage relative to CERES *TRMM* (which sampled all solar zenith angles every 46 days), means that angular sampling at a particular solar zenith angle is increased by at least an order-of-magnitude for CERES *Terra* compared to CERES *TRMM*.

To construct ADMs for *Terra*, 24 months (March 2000–February 2002) of the CERES *Terra* Edition2A Single Scanner Footprint TOA/Surface Fluxes and Clouds (SSF) product (Geier et al. 2001) are used. The CERES SSF product combines CERES radiances and fluxes with scene information inferred from coincident MODIS measurements (Barnes et al. 1998) and meteorological fields based on 4D assimilation data. Cloud properties on the CERES *Terra* SSF product are in-

ferred from MODIS pixel measurements using algorithms that are consistent with those used to produce cloud properties from VIRS (Kummerow et al. 1998) on the CERES *TRMM* SSF (Minnis et al. 2003). Aerosol properties are determined from two sources—(i) by applying the algorithm of Ignatov and Stowe (2002) and (ii) directly from the MOD04 aerosol product (Remer et al. 2005). For *Terra* Edition2A SSF, meteorological fields on the SSF are from the Global Modeling and Assimilation Office (GMAO)'s Goddard Earth Observing System (GEOS) Data Assimilation System (DAS) 4.0.3 product (DAO 1996). GMAO is running GEOS DAS V4.0.3 without any code modifications to produce a consistent analysis over the entire CERES data record.

As described in more detail in Loeb et al. (2003a), accurate spatial and temporal matching of imager-derived aerosol and cloud properties with CERES broadband radiation data are obtained by accounting for the CERES point spread function (PSF) (Smith 1994) when averaging imager-derived properties over the CERES footprint. Within a CERES footprint, the properties of every cloudy imager pixel are assigned to a cloud layer. If there is a significant difference in cloud phase or effective pressure within a CERES field of view (FOV), up to two nonoverlapping cloud layers are defined. A single footprint may contain any combination of a clear area and one or two distinct cloud layers (see Fig. 1 of Loeb et al. 2003a). To reduce the processing time needed to generate the CERES SSF product, the CERES team has decided to process only every fourth MODIS pixel from every second scan line. This introduces a random noise in the PSF-weighted average imager reflectance and brightness temperature of approximately 1.5% and 0.2%, respectively, over CERES FOVs (W. F. Miller 2003, personal communication).

3. CERES *Terra* ADM development

TOA flux is the radiant energy emitted or scattered by the earth–atmosphere per unit area. Flux is related to radiance (I) as follows:

$$F(\theta_o) = \int_0^{2\pi} \int_0^{\pi/2} I(\theta_o, \theta, \phi) \cos\theta \sin\theta \, d\theta d\phi, \qquad (1)$$

where θ_o is the solar zenith angle, θ is the observer viewing zenith angle, and ϕ is the relative azimuth angle defining the azimuth angle position of the observer relative to the solar plane. An ADM is a set of anisotropic factors (R) for determining the TOA flux from an observed radiance as follows:

$$F(\theta_o) = \frac{\pi I(\theta_o, \theta, \phi)}{R(\theta_o, \theta, \phi)}. \qquad (2)$$

Because CERES measures the upwelling radiation from a scene at any given time from one or more directions, F (or R) cannot be measured instantaneously. Instead, R is obtained from a set of predetermined empirical ADMs that are defined for several scene types with distinct anisotropic characteristics. For CERES *TRMM*, the ADMs were constructed by the sorting-into-angular-bins (SABs) method (Suttles et al. 1992; Loeb et al. 2003a). In the SAB method, a large ensemble of radiance measurements are first sorted into discrete angular bins and parameters that define an ADM scene type, and ADM anisotropic factors for a given scene type (j) are given by

$$R_j(\theta_{oi}, \theta_k, \phi_l) = \frac{\pi \bar{I}_j(\theta_{oi}, \theta_k, \phi_l)}{F_j(\theta_{oi})}, \qquad (3)$$

where $\bar{I}_j$ is the average radiance (corrected for Earth–sun distance in the SW) in an angular bin (θ_{oi}, θ_k, ϕ_l), and F_j is the upwelling flux in a solar zenith angle bin θ_{oi}, which is determined by directly integrating $\bar{I}_j$ over all angles (Loeb et al. 2003a). The set of angles (θ_{oi}, θ_k, ϕ_l). corresponds to the midpoint of a discrete angular bin defined by [$\theta_{oi} \pm (\Delta\theta_o/2)$, $\theta_k \pm (\Delta\theta/2)$, $\phi_l \pm (\Delta\phi/2)$], where $\Delta\theta_o$, $\Delta\theta$, and $\Delta\phi$ represent the angular bin resolution. To evaluate F_j from satellite measurements, Loeb et al. (2002) showed that the reference level for the satellite viewing geometry must be defined at least 100 km above the earth's surface in order to account for radiation contributions escaping the planet along slant paths above the earth's tangent point. Loeb et al. (2002) also argue that the optimal reference level for defining instantaneous TOA fluxes in Earth radiation budget studies is approximately 20 km. This reference level corresponds to the effective radiative "top of atmosphere" because the radiation budget equation is equivalent to that for a solid body of a fixed diameter that only reflects and absorbs radiation.

For CERES *Terra* these definitions are retained. The SAB method is used to develop ADMs for some, but not all, ADM scene types. As described in more detail in sections 4 and 5, where possible, we have developed ADMs that are continuous functions of imager-based retrievals, using analytical functions to represent the CERES radiance dependence on scene type. As in Loeb et al. (2003a), SW ADMs are defined explicitly as a function of three angles (θ_{oi}, θ_k, ϕ_l), while LW ADMs are assumed to be a function of only viewing zenith angle.

4. SW ADMs

a. Ocean

1) CLEAR

When the MODIS pixel-level cloud coverage within a CERES FOV is $\leq$0.1%, the CERES FOV is defined as being clear. Following the approach used in Loeb et al. (2003a), instantaneous TOA fluxes are determined using a combination of empirical and theoretical ADMs as follows:

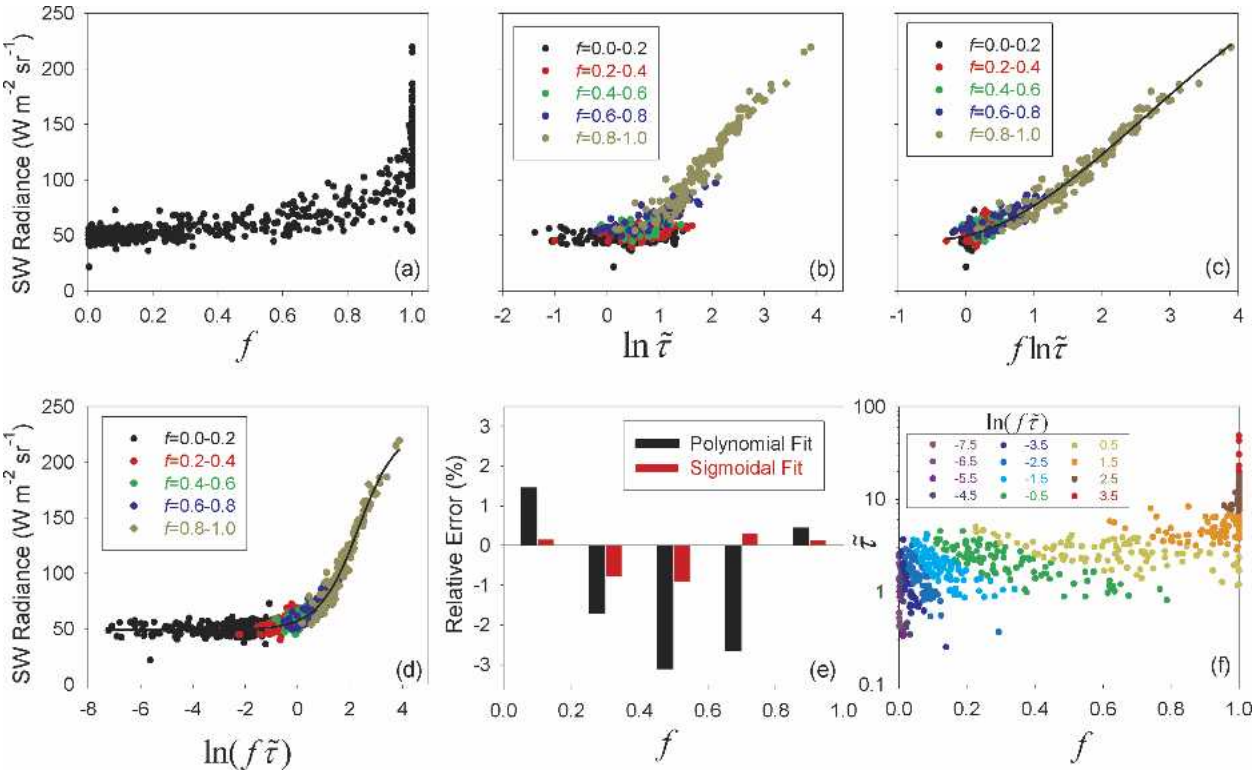

FIG. 1. Instantaneous CERES SW radiances for liquid water cloud layers in the angular bin defined by θ_o = 34°–36°, θ = 50°–52°, and ϕ = 6°–8° against (a) cloud fraction (f); (b) mean logarithm of cloud optical depth ($\ln\tilde{\tau}$); (c) $f\ln\tilde{\tau}$; and (d) $\ln(f\tilde{\tau})$. Solid lines in (c) and (d) correspond to a third-order polynomial fit and a five-parameter sigmoid fit, respectively. (e) Relative error in the fits for different intervals of cloud fraction and (f) $\ln(f\tilde{\tau})$ against f and $\tilde{\tau}$.

$$\hat{F} = \frac{\pi I(\theta_o, \theta, \phi)}{R(w_k, \theta_o, \theta, \phi)\left[\dfrac{R^{\text{th}}(w_k, I)}{R^{\text{th}}(w_k, \bar{I})}\right]}, \tag{4}$$

where $R(w_k, \theta_o, \theta, \phi)$ is determined from wind speed–dependent empirical ADMs that are derived from CERES data, and $R^{\text{th}}(w_k, I)$ and $R^{\text{th}}(w_k, \bar{I})$ are theoretical radiative transfer model anisotropic factors evaluated at the measured CERES radiance $I(\theta_o, \theta, \phi)$ and mean CERES radiance $\bar{I}(w_k, \theta_o, \theta, \phi)$ in a given ADM angular bin, respectively. For *Terra*, the angular bin resolution of the clear ocean SW ADMs has been sharpened to 2° (CERES *TRMM* used 10° for θ_o and θ, and 20° for ϕ), and the wind speed resolution has been increased to 2 m s^{-1} for winds ranging from 0 to 12 m s^{-1} (the nominal wind speed intervals for CERES *TRMM* were <3.5, 3.5–5.5, 5.5–7.5, and >7.5 m s^{-1}). Wind speeds correspond to the 10-m level based on Special Sensor Microwave Imager (SSM/I) retrievals (Goodberlet et al. 1990) that have been ingested into the GEOS-4 DAS analysis. To determine $R^{\text{th}}(w_j, I)$ and $R^{\text{th}}(w_j, \bar{I})$, CERES radiances $I(\theta_o, \theta, \phi; h_{\text{sfc}})$ and $\bar{I}(\theta_o, \theta, \phi; h_{\text{sfc}})$ are compared with lookup tables of theoretical SW radiances stratified by aerosol optical depth. Here, $R^{\text{th}}(w_j, I)$ and $R^{\text{th}}(w_j, \bar{I})$ correspond to the aerosol optical depth for which the theoretical radiances match the CERES radiances. The radiative transfer calculations are from the rstar5b radiative transfer model that is based on Nakajima and Tanaka (1986, 1988). Maritime aerosols from Hess et al. (1998) evaluated at 26 optical depths are used to produce the lookup tables. The ocean surface in the calculations accounts for the bidirectional reflectance of the ocean at wind speeds that correspond to the midpoints of the CERES ADM wind speed intervals.

2) CLOUDS

The CERES *TRMM* ADMs were developed for discrete scene types defined by cloud phase (two categories), cloud fraction (12 intervals), and cloud optical depth (14 intervals). Because of the close spatial and temporal coincidence between CERES radiances and imager-derived parameters over a CERES FOV, an alternate approach is to construct continuous ADMs using analytical functions that relate CERES radiances and imager parameters. For clouds, the magnitude of CERES radiances in an angular bin is most sensitive to cloud fraction and cloud optical depth. To illustrate, Figs. 1a and 1b show instantaneous CERES SW radiances in the angular bin, defined by θ_o = 34°–36°;

$\theta = 50°–52°$; $\phi = 6°–8°$ against cloud fraction (f) (Fig. 1a) and the mean logarithm of cloud optical depth ($\ln\tilde{\tau}$) (Fig. 1b) for liquid water cloud layers. Here, $\tilde{\tau}$ is defined by

$$\tilde{\tau} = \exp(\overline{\ln\tau_i}), \tag{5}$$

and τ_i is the retrieved cloud optical depth of the ith pixel within the CERES FOV. Four months (November–December 2000, April–May 2001) of SSF data are considered in Fig. 1. Equation (5) follows from Cahalan et al. (1994), who showed that for overcast conditions albedo is approximately linear in $\overline{\ln\tau_i}$ when either the variability in the cloud optical depth field is small or the curvature in the albedo $\overline{\ln\tau_i}$ relation is small. When both overcast and broken cloud fields are considered, the SW radiance dependence on f and $\ln\tilde{\tau}$ shows a lot of scatter (Figs. 1a–b). To improve the relationship, we seek to combine f and $\ln\tilde{\tau}$ into a single parameter. Figures 1c and 1d show results for two candidates: (i) $\ln\tilde{\tau}$ weighted by cloud fraction over a CERES FOV, and (ii) the logarithm of $\tilde{\tau}$ weighted by cloud fraction, respectively. Mathematically, these are expressed as

$$\ln\tilde{\tau}_1^{\mathrm{FOV}} = f\ln\tilde{\tau} = f\,\overline{\ln\tau_i}, \tag{6}$$

$$\ln\tilde{\tau}_2^{\mathrm{FOV}} = \ln(f\tilde{\tau}) = \ln f + \overline{\ln\tau_i}. \tag{7}$$

In Fig. 1c, a third-order polynomial fit (solid black line) is applied to data points, while Fig. 1d applies a five-parameter sigmoidal fit, defined by

$$I = I_o + \frac{a}{[1 + e^{-(x-x_o/b)}]^c}, \tag{8}$$

where x_o, I_o, a, b, c are coefficients of the fit, and $x = \ln(f\tilde{\tau})$. The relative error in the fits for different intervals of cloud fraction is shown in Fig. 1e. The sigmoidal fit relative error remains less than 1% in every cloud fraction interval, while it reaches −3% at intermediate cloud fractions using the polynomial fit. The relative root-mean-square (rms) error for the two fits is similar, approximately 8.7% for the polynomial fit and 8.6% for the sigmoidal fit. Similar results are obtained when other angular bins are considered or when separate fits are derived for mixed-phase and ice clouds (not shown). In general, the rms error in predicting instantaneous SW radiances using the sigmoidal fit is between 5% and 10%. The close relationship between SW radiance and $\ln(f\tilde{\tau})$ occurs in spite of the rather large range of cloud properties associated with a given $\ln(f\tilde{\tau})$ range. This is illustrated in Fig. 1f, which shows $\ln(f\tilde{\tau})$ against f and $\tilde{\tau}$ [in $\ln(f\tilde{\tau})$ increments of 1]. At intermediate $\ln(f\tilde{\tau})$ (e.g., from 0 to 1), f varies by as much as 0.8 (e.g., from 0.2 to 1.0) and $\tilde{\tau}$ varies by 4 (e.g., from 1 to 5). In contrast, the corresponding SW radiance variability is only 8.5%.

CERES *Terra* ADMs are determined from sigmoidal fits between SW radiance and $\ln(f\tilde{\tau})$ in 2° angular bins (i.e., 2° resolution for θ_o, θ, and ϕ) as a function of cloud phase. Cloud phase is represented by an effective cloud phase (ECP) index (Loeb et al. 2003a), which is a PSF-weighted average of cloud phase derived from imager pixel data (1 = liquid water, and 2 = ice). For CERES *TRMM*, "liquid clouds" were defined as footprints with ECP < 1.5, and "ice clouds" were defined as footprints with ECP ≥ 1.5. For CERES *Terra*, ADMs are defined for three categories of cloud phase: liquid water (1.00 < ECP < 1.01), mixed phase (1.01 ≤ ECP ≤ 1.75), and ice (1.75 < ECP ≤ 2.00).

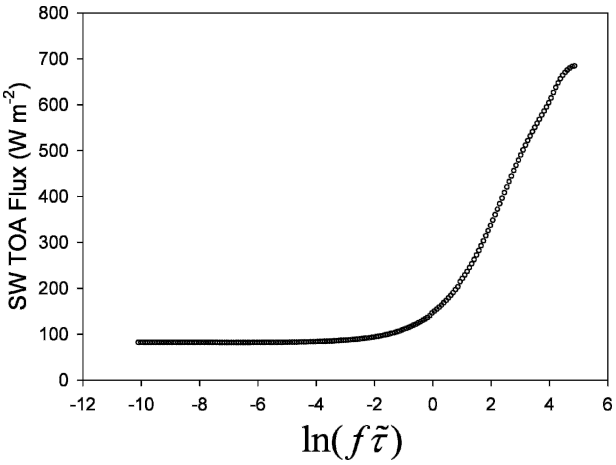

FIG. 2. TOA flux against $\ln(f\tilde{\tau})$ for liquid water clouds at θ_o = 44°–46°.

In angular bins where sunglint is strong (i.e., within 20° of the specular reflection direction), sigmoidal fits are defined only for thick clouds [$\ln(f\tilde{\tau}) \geq 1.4$ or $f\tilde{\tau} \geq 4$]. For thin clouds in sunglint, SW radiances are averaged in four discrete intervals of $\ln(f\tilde{\tau})$. To determine sigmoidal fits using all of the available CERES *Terra* measurements (i.e., 24 months), CERES SW radiances are first averaged in 750 intervals of $\ln(f\tilde{\tau})$ between −10 and 5. The TOA flux in each $\ln(f\tilde{\tau})$ interval is obtained by integrating SW radiances inferred from the fits in all upwelling directions. Figure 2 shows an example of TOA flux against $\ln(f\tilde{\tau})$ for liquid water clouds at θ_o = 44°–46°. Anisotropic factors at a given value of $\ln(f\tilde{\tau})$ are determined from an expression similar to Eq. (3), using sigmoidal fits to infer radiances and lookup tables of SW TOA flux as a function of solar zenith angle and $\ln(f\tilde{\tau})$.

Figures 3a and 3b show CERES SW anisotropic factors in the principal plane for liquid water (Fig. 3a) and ice clouds (Fig. 3b) at $\ln(f\tilde{\tau}) = 2.01$ (or $f\tilde{\tau} = 7.5$) for three solar zenith angle intervals based on 24 months of CERES *Terra* measurements. In each solar zenith angle interval, the liquid water clouds show well-defined peaks in anisotropy for $\theta = -30°$ to $-60°$ and close to nadir due to the cloud glory and rainbow features, respectively, while peaks in anisotropy occur for ice clouds between $\theta = 30°$ and 60° in the specular reflection direction. Chepfer et al. (1999) also observed

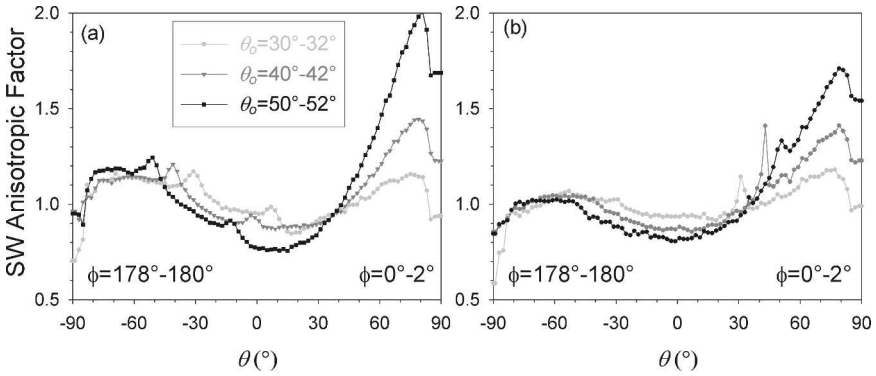

FIG. 3. CERES SW anisotropic factors in the principal plane for (a) liquid water and (b) ice clouds at $\ln(f\tilde{\tau}) = 2.01$ (or $f\tilde{\tau} = 7.5$) for three solar zenith angle intervals based on 24 months of CERES *Terra* measurements (negative θ corresponds to $\phi = 178°$–$180°$; positive θ corresponds to $\phi = 0°$–$2°$).

these features in multiangle Polarization and Directionality of Earth Reflectances (POLDER) measurements and showed theoretically that these are likely due to horizontally oriented ice crystals. Such pronounced microphysical features were not present in ERBE and CERES *TRMM* ADMs because the angular bins used to define those ADMs were too coarse.

b. Land and desert ADMs

1) CLEAR

Over clear land and desert, the CERES *TRMM* ADMs were defined by grouping the International Geosphere Biosphere Program (IGBP) global land cover types (Loveland and Belward 1997) over the Tropics into four categories: low-to-moderate tree/shrub coverage, moderate-to-high tree/shrub coverage, dark desert, and bright desert. These categories were assumed to apply over extensive geographical areas and remain invariant throughout the year. On a global scale, this classification is inadequate because it does not account for vegetation types outside of the Tropics, many of which exhibit strong seasonal variations. To improve the spatial resolution of the clear land and desert ADMs and account for changes in surface type with season, the *Terra* ADMs over clear land and desert are defined for 1° latitude × 1° longitude equal area regions, with a temporal resolution of 1 month. To generate ADMs at these scales, all snow-free, clear-sky CERES *Terra* SW radiances from the available 24 months of SSF data are first sorted by calendar month and 1° latitude × 1° longitude equal area region. Each FOV radiance is converted to a reflectance as follows:

$$r(\theta_o, \theta, \phi) = \frac{\pi I(\theta_o, \theta, \phi)}{\mu_o E_o}(1 + \varepsilon_{se})^2, \tag{9}$$

where $\mu_o = \cos\theta_o$, E_o is the TOA solar irradiance ($=1365$ W m^{-2}) and $(1 + \varepsilon_{se})$ is the Earth–sun distance in astronomical units (AUs). A TOA normalized vegetation difference index (NDVI) for each CERES FOV is determined from PSF-weighted mean MODIS 0.63- ($\bar{I}_{0.63}$) and 0.86-μm ($\bar{I}_{0.86}$) radiances as follows:

$$\text{NDVI} = \frac{\bar{I}_{0.86} - \bar{I}_{0.63}}{\bar{I}_{0.86} + \bar{I}_{0.63}}. \tag{10}$$

The TOA NDVI is used to separate subregions within a 1° latitude × 1° longitude region that have different vegetation characteristics. Subregions with TOA NDVI differing by 0.1 or more are treated separately. Next, if angular sampling within a region is sufficient, an eight-parameter nonparametric fit from Ahmad and Deering [1992, see their Eq. (37)] is applied to the CERES SW reflectances to represent the angular dependence in the reflectance field. The Bidirectional Reflectance Distribution Function (BRDF) used in the fit accounts for multiple scattering based on Chandrasekhar's (1950) radiative transfer solution for a semi-infinite medium, and the so-called "hot spot" is modeled using an empirical term (Hapke 1986). Separate fits are derived for every 0.2 increment in μ_o, provided that at least three CERES FOVs are available in the following geometries: (i) $\theta \le 20°$, (ii) $\theta \ge 40°$ and $\phi \le 30°$, (iii) $\theta \ge 40°$ and $60° \le \phi \le 120°$, and (iv) $\theta \ge 40°$ and $\phi \ge 150°$. If this condition is not satisfied, then CERES FOVs from neighboring regions with the same IGBP type, NDVI and μ_o intervals are used to supplement the angular sampling. Only FOVs from neighboring regions within ±15° latitude × ±15° longitude are considered. If the viewing angle sampling criterion is still not satisfied, then a fit is not performed, and fluxes are determined using the CERES *TRMM* ADMs.

Figures 4a and 4b show the regional relative rms error when the BRDF fits are applied to RAP and cross-track CERES data from December 2000 through February 2001 (Fig. 4a), and from June 2000 through August 2000 (Fig. 4b). Histograms of relative error and relative rms error are provided in Figs. 5a–b. Overall, the relative rms error in reflectance from the BRDF fit

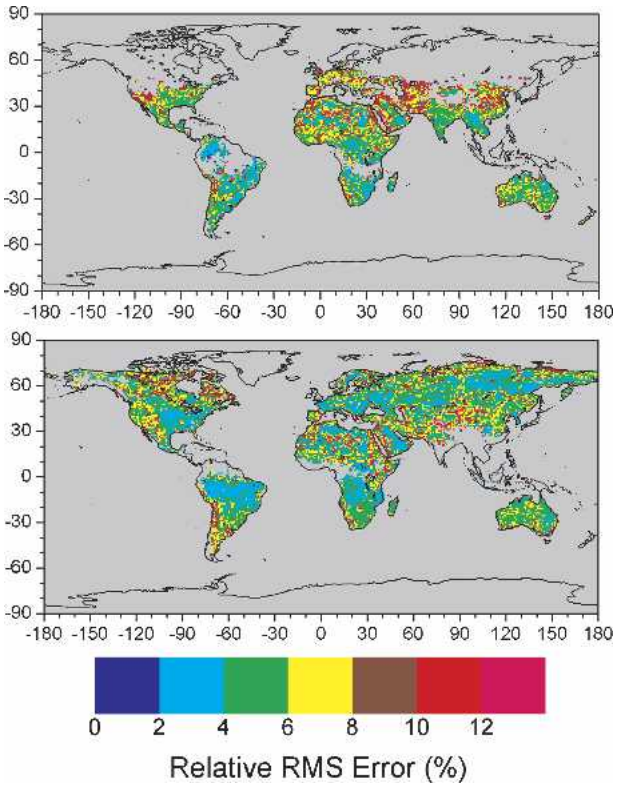

FIG. 4. Regional relative rms error in BRDF fits for RAP and cross-track CERES data from (a) Dec 2000 through Feb 2001 and (b) Jun 2000 through Aug 2000.

is between 6% and 7% for the two seasons. Relative errors tend to be larger over mountainous regions (e.g., Rockies, Andes, Tibetan Plateau) and smaller over the broadleaf forest regions of South America and over the central United States in summer.

To construct an ADM from the BRDF fits, albedos at several solar zenith angles in the interval of μ_o, in which the BRDF fit was derived, are first computed by directly integrating the BRDFs over θ and ϕ. Next, a fit based on Rahman et al. (1993) is used to represent the albedo dependence on solar zenith angle in each μ_o interval. The instantaneous anisotropic factor at a given

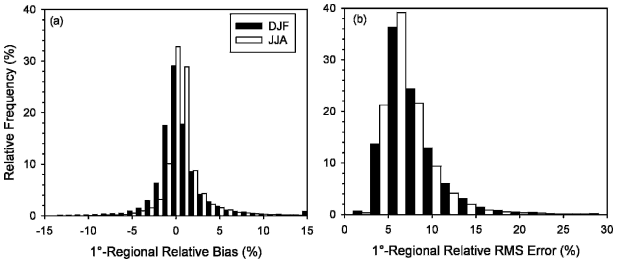

FIG. 5. Histograms of (a) 1° regional relative bias and (b) 1° regional relative rms error in BRDF fits for RAP and cross-track CERES data from Dec 2000 through Feb 2001, and Jun 2000 through Aug 2000.

location is inferred from the ratio of reflectance to albedo, both of which are evaluated from the above fits at the FOV viewing geometry.

2) CLOUDS

The anisotropy of clouds over land and desert depends strongly upon cloud phase, cloud fraction, cloud optical thickness, and the underlying surface type (especially in thin or broken cloud conditions). CERES *TRMM* ADMs for clouds over land and desert were defined for discrete classes of cloud phase, cloud fraction, and cloud optical depth for the four surface types that were used to define clear land CERES *TRMM* ADMs. For CERES *Terra*, we use a similar approach to that outlined over the ocean [section 4b(2)], with an additional correction to account for surface reflection. Following Arking and Childs (1985), an observed radiance (I) is modeled as follows:

$$I(\mu_o, \mu, \phi) = (1 - f)\frac{\mu_o E_o}{\pi}\rho^{\text{clr}}(\mu_o, \mu, \phi) + fI^{\text{cld}}(\mu_o, \mu, \phi) + f\frac{\mu_o E_o}{\pi}\left[\rho^{\text{clr}}(\mu_o, \mu, \phi)\, e^{-\tau/\mu_o}\, e^{-\tau/\mu} + \overline{\alpha}^{\text{clr}}\frac{t^{\text{cld}}(\tau, \mu_o)t^{\text{cld}}(\tau, \mu)}{1 - \overline{\alpha}^{\text{clr}}\overline{\alpha}^{\text{cld}}(\tau)}\right], \quad (11)$$

where the first term corresponds to reflection from the cloud-free area, the second term represents reflection from the cloud, and the third and fourth terms correspond to scattering by the surface and atmosphere transmitted through the cloud, respectively; ρ^{clr} is the clear-sky bidirectional reflectance, $\mu = \cos\theta$, I^{cld} is the radiance from the cloud layer, τ is the cloud optical depth, $\overline{\alpha}^{\text{clr}}$ and $\overline{\alpha}^{\text{cld}}$ are the clear-sky and cloud spherical albedos (Thomas and Stamnes 1999), respectively, and t^{cld} is the diffuse transmittance of the cloud. Respectively, ρ^{clr} and $\overline{\alpha}^{\text{clr}}$ are inferred from 1° BRDF fits; $\overline{\alpha}^{\text{cld}}$ and t^{cld} are determined from broadband radiative transfer model calculations using a highly modified version of the model described in Fu and Liou (1993). In the radiative transfer model calculations, liquid water clouds are assumed to have an effective droplet radius of 10 μm, and ice clouds are assumed to have an effective particle diameter of 60 μm. Lookup tables of $\overline{\alpha}^{\text{cld}}$ and t^{cld} are generated at 17 solar zenith angles and 19 cloud optical depths.

Because I is known from the observations, Eq. (11) can be used to estimate the contribution from the cloudy area (fI^{cld}). Figure 6a shows an example of fI^{cld} against $\ln(f\tilde{\tau})$ for the angular bins $\theta_o = 40°$–$45°$, $\theta = 0°$–$5°$, and $\phi = 0°$–$5°$. To generate this curve, all CERES measurements from 24 months for all land and desert types were included and CERES radiances were averaged in 375 intervals of $\ln(f\tilde{\tau})$. The relative rms error in the sigmoid fit (solid line) is approximately 7%,

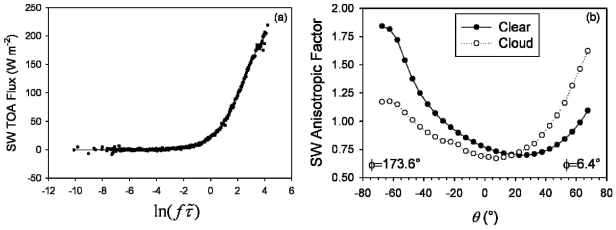

FIG. 6. (a) Cloud SW radiance (fI^{cld}) against ln($f\tilde{\tau}$) for clouds over land and desert in angular bins θ_o = 40°–45°, θ = 0°–5°, and ϕ = 0°–5°. Solid line is a five-parameter sigmoid fit to the data. (b) Sample ADMs for clear and cloudy conditions over a cropland/natural vegetation mosaic surface (latitude = 36.52°N, longitude = 128.72°E) for θ_o = 59.24° on 2 Dec 2000. The cloud is composed of liquid water, covers 74% of the CERES FOV, and has a cloud optical depth of 5.2.

comparable to what was obtained for clouds over the ocean. Sigmoidal fits were also determined in all other angular bins where CERES *Terra* observations occur. An angular resolution of 5° in θ_o, θ, and ϕ is used for land and desert. Separate fits were derived for liquid water, and mixed and ice clouds, defined in section 4a(2). Using fI^{cld}, predicted from the sigmoidal fits together with the 1° latitude × 1° longitude monthly clear land BRDF fits described in section 4b(1), the approximation in Eq. (11) is used to construct ADMs for clouds over land and desert that account for regional and seasonal changes in surface properties. The ADM flux is inferred by integrating Eq. (11):

$$F(\mu_o) = (1-f)\mu_o E_o \alpha^{\mathrm{clr}}(\mu_o) + \int_0^{2\pi}\int_0^1 fI^{\mathrm{cld}}(\mu_o, \mu, \phi)\mu\, d\mu d\phi + f\mu_o E_o \left[\alpha^{\mathrm{clr}}(\mu_o)\, \mathrm{e}^{-\tau/\mu_o} 2 \int_0^1 \mathrm{e}^{-\tau/\mu}\mu d\mu + \overline{\alpha}^{\mathrm{clr}} \frac{t^{\mathrm{cld}}(\tau, \mu_o)\bar{t}^{\mathrm{cld}}(\tau)}{1 - \overline{\alpha}^{\mathrm{clr}}\overline{\alpha}^{\mathrm{cld}}(\tau)} \right], \quad (12)$$

where α^{clr} is the plane albedo and $\bar{t}^{\mathrm{cld}}$ is the spherical transmittance (ratio of transmitted flux to incident flux for an isotropic source). To reduce computation time, we assume $\rho^{clr}(\mu_o, \mu, \phi) \approx \alpha^{\mathrm{clr}}(\mu_o)$ in the third term of Eq. (12), thereby avoiding explicit double integration over $\rho^{\mathrm{clr}}(\mu_o, \mu, \phi)\, \mathrm{e}^{-\tau/\mu}$ for every CERES FOV.

An anisotropic factor for an arbitrary FOV is determined from radiance and flux estimates using Eqs. (11) and (12) with the appropriate clear-sky 1° BRDF fits and sigmoidal curve. Figure 6b provides sample ADMs for clear and cloudy conditions over a cropland/natural vegetation mosaic surface (latitude = 36.52°N, longitude = 128.72°E) for θ_o = 59.24° on 2 December 2000. The cloud is composed of liquid water, covers 74% of the CERES FOV, and has a cloud optical depth of 5.2. The clear-sky case shows a markedly stronger backscatter contribution compared to the cloud case, which scatters more radiation into the forward direction owing to its scattering phase function characteristics.

c. Snow and sea ice

One of the major differences in angular distribution model development for *Terra* compared with *TRMM* is the availability of CERES RAP data over polar regions. Because the *TRMM* orbit is restricted to tropical latitudes, there were not enough data to develop empirical snow ADMs for CERES *TRMM*. As a result, Loeb et al. (2003a) used theoretical ADMs to infer TOA fluxes over snow in tropical regions. Because *Terra* is a sun-synchronous polar-orbiting satellite, CERES instruments on *Terra* measure radiances in polar regions from various scene types and a wide range of viewing geometries. This allows the development of empirical ADMs to estimate radiative fluxes from snow and sea ice.

For convenience, snow/ice surfaces are divided into three groups: permanent snow, fresh snow, and sea ice. Most permanent snow scenes occur over Antarctica and Greenland, whereas fresh snow and sea ice occur over land and water, respectively. Because anisotropy also varies with surface brightness (Loeb et al. 2003a), each of the three surface types are further stratified into "bright" and "dark" subclasses. A CERES FOV is determined to be bright or dark by comparing its geographical location with a predetermined monthly regional snow map that classifies all 1° × 1° regions with snow/sea ice as either bright or dark (Kato and Loeb 2005). The snow maps are constructed as follows. (i) Using all available cloud-free CERES FOVs with snow/sea ice, mean MODIS 0.63-μm near-nadir (for $\theta < 25°$) reflectances are determined as a function of snow type and solar zenith angle; (ii) every CERES FOV whose MODIS 0.63-μm near-nadir reflectance lies below (above) the corresponding mean reflectance is assigned a value of −1 (+1); (iii) if the sum of all CERES FOV classifications in a 1° × 1° region from 1 month of data is negative (positive), the region is classified as dark (bright). In this manner, 12 snow maps representing each calendar month are produced.

To account for the effects of partial coverage by fresh snow or sea ice within a CERES FOV on anisotropy, bright and dark fresh snow and sea ice ADMs are further stratified into six intervals of fresh snow or sea ice percent coverage. When clouds are present, ADMs are further stratified by cloud fraction and cloud optical thickness. Table 1 shows how the snow and sea ice ADMs are defined for each surface type. The total number of ADMs is 10 for permanent snow, 25 for fresh snow, and 25 for sea ice.

Following Loeb et al. (2003a), radiances measured by CERES instruments are sorted into angular bins and averaged. Angular bin sizes are 2° for the solar zenith angle, and 5° for both viewing zenith and relative azimuth angles over permanent snow. For fresh snow and sea ice, angle bin sizes are 5° for all three angles. Radiances in undersampled angular bins are in-

TABLE 1. SW ADM scene-type definitions for permanent snow, fresh snow, and sea ice.

Surface type	Cloud fraction	Surface brightness	Snow/sea ice fraction	Cloud optical thickness
Permanent snow (10)	0.0–0.001	Bright, dark	—	—
	0.001–0.25	All	—	—
	0.25–0.50			
	0.50–0.75			
	0.75–0.999			
	0.999–1.0	Bright, dark	—	Thin ($\tau \leq 10$), thick ($\tau > 10$)
Fresh snow (25), sea ice (25)	0.0–0.01	All	0–0.01	—
			0.01–0.25	
			0.25–0.50	
			0.50–0.75	
			0.75–0.99	
		Bright, dark	0.99–1.0	—
	0.01–0.25	All	0.0–0.01	—
			0.01–0.25	
			0.25–0.50	
			0.50–0.75	
			0.75–0.99	
	0.25–0.50	All	0.0–0.01	—
			0.01–0.25	
			0.25–0.50	
			0.50–0.75	
	0.50–0.75	All	0.0–0.01	—
			0.01–0.25	
			0.25–0.50	
	0.75–0.99	All	0.0–0.01	—
			0.01–0.25	
	0.99–1.0	Bright, dark	—	Thin ($\tau \leq 10$), thick ($\tau > 10$)

ferred using the approach outlined in Loeb et al. (2003a).

Figures 7a–c show SW anisotropic factors for permanent snow (Fig. 7a), fresh snow (Fig. 7b), and sea ice (Fig. 7c) as a function of θ for $\phi = 0°$–$10°$ and $\phi = 170°$–$180°$. When clouds are present over snow/sea ice, SW anisotropic factors show a greater dependence on viewing zenith angle than cloud-free scenes, especially in the forward scattering direction. Anisotropic factors for clear bright and dark surfaces are remarkably similar over permanent snow, while the brighter surfaces tend to be slightly more isotropic than dark scenes over fresh snow and sea ice.

d. Mixed-scene fields of view

Shortwave anisotropic factors for CERES FOVs that lie over water–land–snow boundaries are determined by accounting for the fractional coverage by each surface type as follows:

$$R(\theta_o, \theta, \phi) = \frac{\pi(f_W \bar{I}_W + f_L \bar{I}_L + f_S \bar{I}_S)}{f_W F_W + f_L F_L + f_S F_S}, \qquad (13)$$

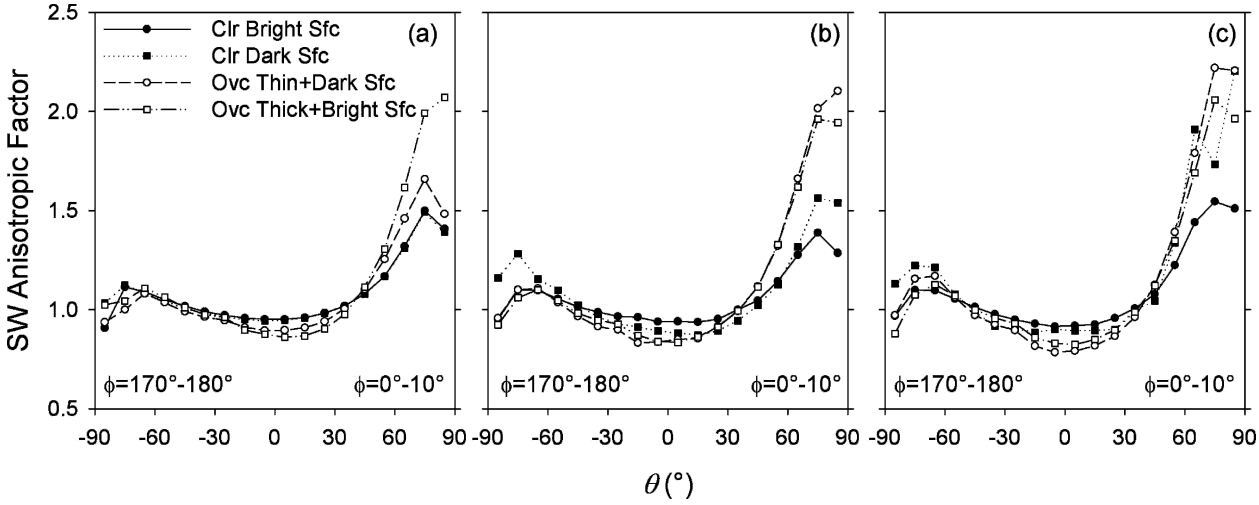

FIG. 7. SW anisotropic factors against CERES viewing zenith angle near the principal plane for (a) permanent snow for $\theta_o = 62°$–$64°$; (b) fresh snow for $\theta_o = 60°$–$65°$; and (c) sea ice for $\theta_o = 60°$–$65°$. "Clr" corresponds to clear; "Ovc" corresponds to overcast.

where f_W, f_L, and f_S correspond to the fractional coverage over a CERES FOV by water, land, and snow, respectively; and $\bar{I}_X$ and F_X ($X = W, L, S$) are the mean radiance and TOA flux used to define ADMs for FOVs with 100% coverage by water, land, or snow.

e. Sunglint conditions

When a CERES FOV is over water and the satellite viewing geometry is near the specular reflection direction, the radiance-to-flux conversion is less reliable owing to the large variability in ocean reflectance at those angles. To determine whether or not a footprint is too close to the specular reflection direction to provide a reliable flux retrieval, the following expression is evaluated:

$$\sigma_R = (1 - f_{\text{ice}} - f_{\text{cld}})\sigma_{R_{\text{clr}}}, \tag{14}$$

where f_{ice} and f_{cld} correspond to the fraction of the CERES FOV covered by sea ice and cloud, respectively, and $\sigma_{R_{\text{clr}}}$ is the standard deviation of clear ocean anisotropic factors in angular bins adjacent to the observation angle. If an observation falls in an angular bin for which $\sigma_R \geq 0.05$, a radiance-to-flux conversion is not performed. Instead, a mean flux value, corresponding to the ADM scene type over the FOV, is used. ADM flux values are determined when the ADMs are constructed by direct integration of the radiances for the corresponding scene type.

5. LW and WN ADMs

ADMs for LW and WN scenes are defined in terms of several surface and meteorological properties that influence radiance anisotropy over the ocean, land, and desert. In addition, because the cloud retrieval algorithm uses different approaches during the daytime and nighttime owing to the lack of visible imager information at night, separate LW and WN ADMs are developed for daytime and nighttime conditions.

a. Clear ocean, land, and desert

To account for the increased variability in surface properties encountered by *Terra* compared to *TRMM*, the number of surface types used to define land and desert ADMs has been increased from two for *TRMM* to six for *Terra*. Table 2 provides the IGBP surface types corresponding to each of the six land categories. These classes were determined by analyzing the spatial distribution of surface emissivity (Wilber et al. 1999) over the different IGBP types.

In addition to surface type, the scene types are stratified into discrete intervals of precipitable water (w), vertical temperature change (ΔT), and imager-based surface skin temperature (T_s) (Table 3). Over water, w is obtained from SSM/I retrievals; over land and desert, w is obtained from meteorological values (DAO 1996). Here, ΔT is defined as the lapse rate in the first 300 hPa of the atmosphere above the surface. It is computed by subtracting the DAO (1996) air temperature at the pressure level that is 300 hPa below the surface pressure (i.e., surface pressure minus 300 hPa) from T_s; T_s is estimated from the clear-sky 11-μm radiance using a narrowband radiative transfer algorithm that uses temperature and humidity profile inputs from the GEOS DAS V4.0.3 (Minnis et al. 2003).

TABLE 2. Surface-type definitions for clear-sky LW and WN ADMs over the ocean, land, and desert.

ADM surface type	IGBP type
Forests	(1) Evergreen needleleaf (2) Evergreen broadleaf (3) Deciduous needleleaf (4) Deciduous broadleaf (5) Mixed
Savannas	(8) Woody savannas (9) Savannas
Grasslands/cropland	(6) Closed shrubland (10) Grasslands (11) Permanent wetlands (12) Croplands (13) Urban (14) Cropland/natural vegetation mosaics
Dark deserts	(7) Open shrubland (18) Tundra
Bright deserts	(16) Barren deserts
Ocean	(17) Water bodies

Longwave and WN ADMs are defined as a function of viewing zenith angle using a 2° angular bin resolution. Consequently, variations in anisotropy with solar zenith angle and relative azimuth angle are not accounted for. While this approximation is reasonable for the ocean and for all surface types at night, it breaks down during daytime for land areas with highly variable topography (Minnis and Khaiyer 2000; Minnis et al. 2004).

Figures 8a–d provide examples of LW ADMs for different surface types as a function of surface skin temperature for $w < 1$ and ΔT between 15 and 30 K. For all surface types, LW anisotropy increases as surface skin temperature increases. Because the WN channel is more sensitive to surface skin temperature, WN anisotropy (not shown) is found to be significantly more pronounced than LW anisotropy. While LW and WN an-

TABLE 3. Precipitable water (w), lapse rate (ΔT), and surface skin temperature (T_s) intervals used to determine LW and WN ADMs under clear-sky conditions over the ocean, land, and desert.

w (cm)	ΔT (K)	T_s (K)
0–1	<15	<270
1–3	15–30	270–290
3–5	30–45	290–310
>5	>45	310–330
		>330

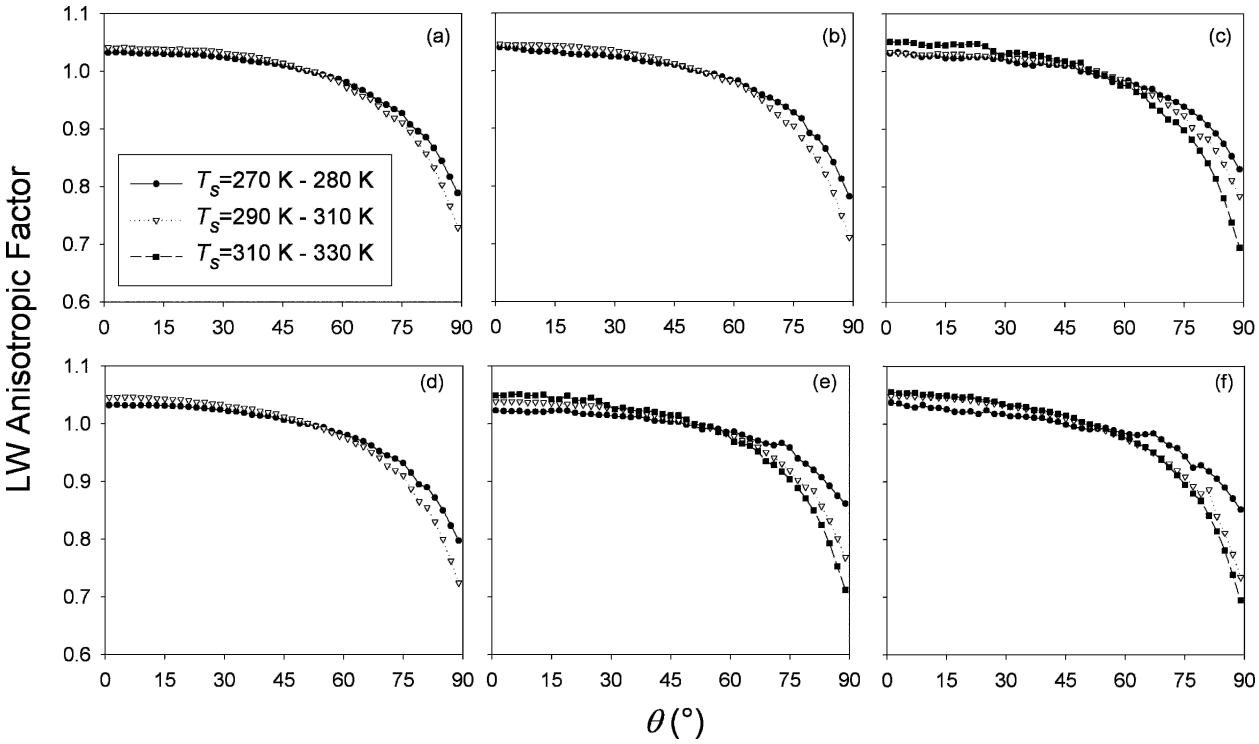

FIG. 8. LW anisotropic factors for clear scenes with w = 0.0–1.0 cm and ΔT = 15°–30°C; (a) ocean, (b) forests, (c) savannas, (d) cropland/grassland, (e) dark deserts, and (f) bright deserts.

isotropy also increases with ΔT, the sensitivity is less pronounced than it is to T_s.

b. Clouds over the ocean, land, and desert

Under cloudy conditions, LW and WN anisotropy depends on several parameters, including surface type, w, T_s, surface–cloud temperature difference ($\Delta T_{\rm sc}$), cloud fraction, and cloud infrared emissivity (ε_c). To characterize scenes in terms of these parameters, we define a "pseudoradiance" parameter ψ as follows:

$$\psi(w, T_s, T_c, f, \varepsilon_s, \varepsilon_c) = (1 - f)\varepsilon_s B(T_s) + \sum_{j=1}^{2} [\varepsilon_s B(T_s)(1 - \varepsilon_{c_j}) + \varepsilon_{c_j} B(T_{c_j})] f_j, \quad (15)$$

where f_j is the cloud fraction of the jth cloud layer within a CERES FOV ($f = f_1 + f_2$), T_{c_j} is the corresponding layer cloud-top temperature, ε_s is the surface infrared emissivity, and $B(T) = \pi^{-1}\sigma T^4$, where σ is the Stefan–Boltzmann constant (=5.6696 × 10^{-8} W m^{-2} sr^{-1} deg^{-4}). Here, ε_{c_j} is determined from

$$\varepsilon_{c_j} = 1 - e^{-\tau_{a_j}}, \quad (16)$$

where τ_{a_j} is the infrared absorption cloud optical depth of the jth layer derived using the approach outlined in Minnis et al. (1998) from visible cloud optical depth and particle effective radius retrievals available on the SSF product. For a given surface type, and fixed intervals of w, f, T_s, and $\Delta T_{\rm sc}$ (Table 4), LW (and WN) radiances show a simple monotonic dependence on ψ. As an example, Fig. 9a shows LW radiances against ψ for three different viewing bins over the ocean for $w > 5$ cm, T_s=300–305 K, $\Delta T_{\rm sc}$ >85 K, and f=1.0. To produce Fig. 9a, the observed LW radiances were averaged in 250 ψ bins of a width of 1 W m^{-2} sr^{-1}. Note that because w, f, T_s, and $\Delta T_{\rm sc}$ are held fixed when Eq. (15) is applied, the main source of variation in ψ is from ε_c For an

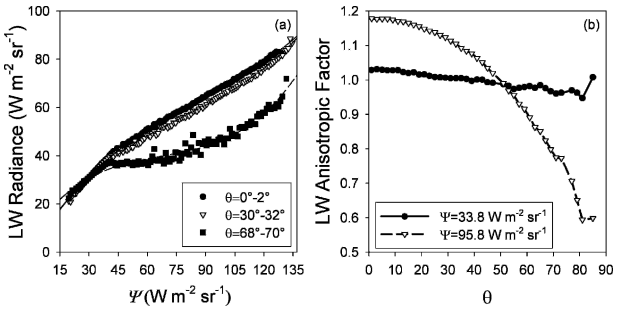

FIG. 9. (a) LW radiance against ψ for θ = 0°–2°, θ = 30°–32°, and θ = 68°–70° over the ocean for $w > 5$ cm, T_s = 300–305 K, $\Delta T_{\rm sc} > 85$ K, and f = 1.0. Solid line corresponds to a third-order polynomial fit to the data. (b) Anisotropic factor (R) against CERES viewing zenith angle for ψ = 33.8 W m^{-2} sr^{-1} and ψ = 95.8 W m^{-2} sr^{-1}.

arbitrary CERES FOV, R is determined by first evaluating the radiance at ψ from Eq. (15) in each viewing zenith angle bin. The relationship between radiance and ψ in a given angular bin is derived from predetermined third-order polynomial fits in each θ bin for the intervals of w, f, T_s, and ΔT_{sc}, shown in Table 4. The radiances are then integrated over viewing zenith angle to produce an ADM flux and R is obtained directly from Eq. (3). Figure 9b shows the viewing zenith angle dependence of R at $\psi = 33.8$ W m^{-2} sr^{-1} and $\psi = 95.8$ W m^{-2} sr^{-1}, corresponding to the conditions in Fig. 9a. At $\psi = 33.8$ W m^{-2} sr^{-1}, the cloud is thick ($\varepsilon_c \approx 1$) and the viewing zenith angle dependence of R is weak. This is expected since the cloud top is located in the upper troposphere where there is less attenuation above the cloud to cause appreciable limb darkening. At $\psi = 95.8$ W m^{-2} sr^{-1}, the clouds are much thinner ($\varepsilon_c \approx 0.4$–$0.5$) and the LW anisotropy is more pronounced because the contribution from the warm ocean surface transmitted through the cloud is attenuated more rapidly with viewing zenith angle.

c. Snow

Longwave and WN ADMs over permanent snow, fresh snow, and sea ice are defined with an angular resolution of 2° in viewing zenith angle for 24 discrete scene classes by clear fraction, surface skin temperature, and surface–cloud top temperature difference (Table 5). Figures 10a–c show daytime LW ADMs for the three surface types. As expected, LW ADMs for clear scenes with $T_s > 250$ K are more anisotropic than those with $T_s \leq 250$ K. Under cloudy conditions, larger anisotropy occurs when $T_s > 250$ K and $\Delta T_{sc} > 20$ K. Clouds in this scene type are not completely opaque close to nadir, so that the difference in the effective temperature at nadir and the oblique viewing angle is large. For $\theta > 84°$, the radiances show more variability because of reduced sampling and because part of the CERES FOV lies beyond the earth's horizon (no scene information is available from the imager over that part of the FOV). The uncertainty in TOA flux due to radiance uncertainties at $\theta > 84°$ is <0.3 W m^{-2}.

6. Footprints with insufficient imager information

In circumstances where there is insufficient imager coverage or scene information for a CERES FOV due to missing MODIS data and/or missing cloud property retrievals, anisotropic factors are determined from the CERES radiances directly using a feed-forward error back-propagation artificial neural network (ANN) simulation (Loukachine and Loeb 2003; Loukachine and Loeb 2004). This occurs when the total fraction of unknown cloud properties over the footprint, as defined by Eq. (2) of Loeb et al. (2003a), is greater than 0.35. The ANN has been trained using CERES *Terra* SSF data to provide a mapping between the CERES radiances and ADM-derived anisotropic factors over different surface types (ocean, land, desert, and snow). Validation tests show that the root-mean-square (rms) difference between instantaneous SW TOA fluxes from the ANN and original ADMs is approximately 9% for SW, 3.5% for LW daytime, and 3% for LW nighttime (WN rms differences are similar). Globally, approximately 5% of CERES TOA fluxes are inferred using the ANN scheme. The frequency of ANN use is significantly higher in mountainous regions, in coastal areas, and over snow/sea ice, where uncertainties in imager-derived cloud properties are larger. ANN is also frequently used at oblique CERES viewing zenith angles in the cross-track direction because MODIS is limited to cross-track viewing zenith angles that are smaller than 63°.

TABLE 4. Surface type, precipitable water (w), cloud fraction (f), surface–cloud temperature difference (ΔT_{sc}), and surface skin temperature (T_s) intervals used to determine LW and WN ADMs under cloudy conditions over the ocean, land, and desert.

Surface type	w (cm)	f	ΔT_{sc} (K)	T_s (K)
Ocean	0–1	0.001–0.5	<−15; −15 to	<275; 275 to
Land	1–3	0.5–0.75	85 every 5 K;	320 every 5 K
Desert	3–5	0.75–0.999	−10–>85	>320
	>5	0.999–1.0		

TABLE 5. Clear fraction (f_{clr}), surface skin temperature (T_s), and surface–cloud temperature difference (ΔT_{sc}) intervals used to determine LW and WN ADMs over permanent snow (PS), fresh snow, and sea ice.

f_{clr}	T_s (K)	ΔT_{sc} (K)
$0.999 < f_{clr} \leq 1.000$	<250	
$0.750 < f_{clr} \leq 0.999$	≥250	<20
$0.500 < f_{clr} \leq 0.750$		≥20
$0.250 < f_{clr} \leq 0.500$	<240 (PS, nighttime)	
$0.100 < f_{clr} \leq 0.250$	≥240 (PS, nighttime)	
$f_{clr} \leq 0.001$		

7. Summary

To determine the earth's radiation budget from CERES, measured radiances at a given sun–Earth–satellite configuration must be converted to outgoing reflected solar and emitted thermal TOA radiative fluxes. CERES SW, LW, and WN ADMs are derived from 24 months of global CERES *Terra* radiances, imager-derived cloud parameters from MODIS, and meteorological information from the Global Modeling and Assimilation Office (GMAO)'s Goddard Earth Observing System Data Assimilation System (DAS) V4.0.3 product. The ADM scene types are defined as a function of scene parameters that have a strong influence on the anisotropy (or angular variation) of the earth's radiation field at the TOA.

For clear scenes over the ocean, CERES *Terra* SW ADMs are defined as a function of wind speed and a

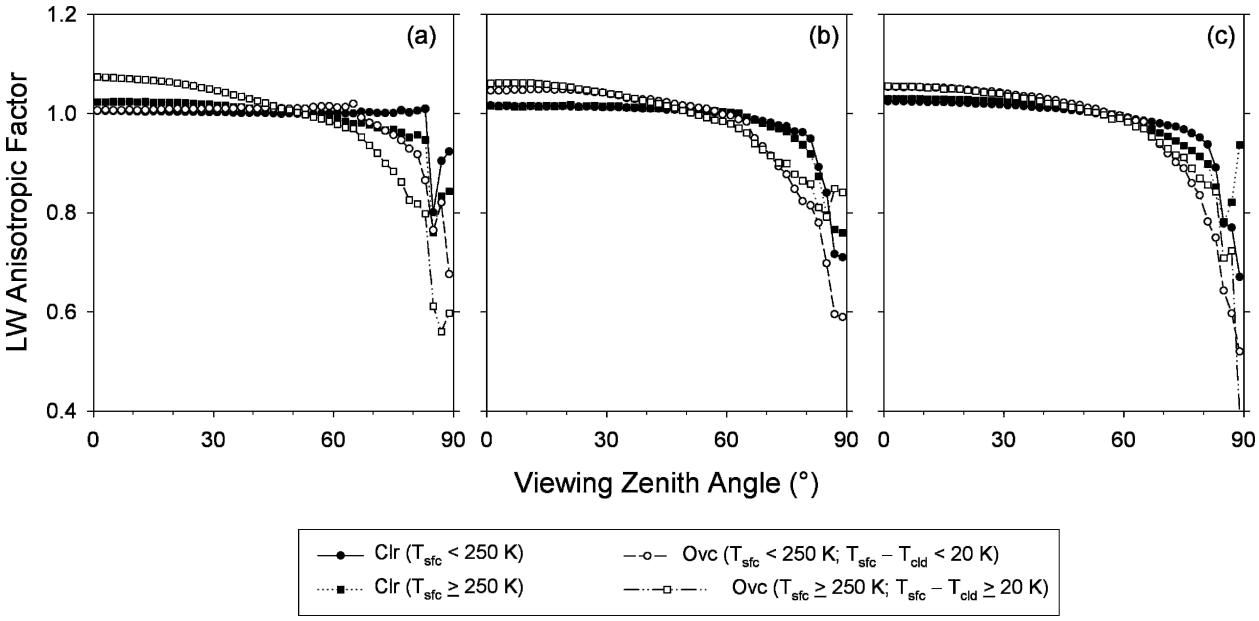

FIG. 10. Daytime LW anisotropic factors against CERES viewing zenith angle for (a) permanent snow, (b) fresh snow, and (c) sea ice. "Clr" corresponds to clear; "Ovc" corresponds to overcast; T_{sfc} refers to surface skin temperature; T_{cld} corresponds to cloud-top temperature.

theoretical correction is used to account for aerosol optical depth variation. Over land and desert, clear ADMs are defined for 1° latitude × 1° longitude equal area regions with a temporal resolution of 1 month. The ADMs are inferred from eight-parameter nonparametric fits to the bidirectional reflectance distribution function at these time and space scales. ADMs for clear scenes over snow/ice surfaces are stratified according to whether the surface is over permanent snow, fresh snow, or sea ice. Each of the three surface types are further stratified into "bright" and "dark" subclasses using predetermined monthly regional snow maps that classify all 1° × 1° regions with snow/sea ice as either bright or dark. Shortwave ADMs under cloudy conditions over the ocean are defined as continuous functions of a cloud parameter determined from imager-based cloud fraction and cloud optical depth. A sigmoidal fit is used to provide a continuous mapping between the cloud parameter and CERES radiances in each 2° angular bin interval in solar zenith angle, viewing zenith angle, and relative azimuth angle. Separate SW ADMs for liquid water, mixed phase, and ice clouds are derived from the sigmoidal fits. A similar approach is used to develop SW ADMs over land and desert, with additional approximations to account for the anisotropy of the underlying surface. ADMs for clouds over snow/ice are defined for discrete classes of cloud fraction and cloud optical thickness.

In the LW and WN regions, ADMs under cloud-free conditions are defined for one ocean class, five land categories corresponding to groupings of major IGBP surface types, and one snow class. The ocean and land clear-sky ADMs are further stratified into discrete intervals of precipitable water, vertical temperature change, and imager-based surface skin temperature. Over snow, clear-sky ADMs are stratified by surface skin temperature. When clouds are present over the ocean, land, or desert, the scene-type dependence of LW and WN radiances is represented by a parameterization that is a function of precipitable water, surface and cloud-top temperature, surface and cloud emissivity, and cloud fraction. Over snow, LW and WN ADMs are defined as a function of cloud fraction, surface skin temperature, and the temperature difference between the surface and cloud top.

In Part II of this paper, SW, LW, and WN TOA fluxes derived from the CERES *Terra* ADMs are assessed through extensive validation tests similar to those described in Loeb et al. (2003b). TOA fluxes from the new *Terra* ADMs will also be compared with TOA fluxes from the CERES *TRMM* ADMs and with fluxes based on algorithms developed during the Earth Radiation Budget Experiment (ERBE) (Smith et al. 1986; Suttles et al. 1992).

Acknowledgments. This research was funded by the Clouds and the Earth's Radiant Energy System (CERES) project under NASA Grant NAG-1-2318.

REFERENCES

Ahmad, S. P., and D. W. Deering, 1992: A simple analytical function for bidirectional reflectance. *J. Geophys. Res.,* **97,** 18 867–18 886.

Arking, A., and J. D. Childs, 1985: Retrieval of cloud cover pa-

rameters from multispectral satellite images. *J. Climate Appl. Meteor.,* **24,** 322–333.
Barnes, W. L., T. S. Pagano, and V. V. Salomonson, 1998: Prelaunch characteristics of the Moderate Resolution Imaging Spectroradiometer (MODIS) on EOS-AM1. *IEEE Trans. Geosci. Remote Sens.,* **36,** 1088–1100.
Cahalan, R. F., W. Ridgway, W. J. Wiscombe, T. L. Bell, and J. B. Snider, 1994: The albedo of fractal stratocumulus clouds. *J. Atmos. Sci.,* **51,** 2434–2455.
Cess, R. D., and Coauthors, 1990: Intercomparison and interpretation of climate feedback processes in 19 atmospheric general circulation models. *J. Geophys. Res.,* **95,** 16, 601–16, 615.
——, and Coauthors, 1996: Cloud feedback in atmospheric general circulation models: An update. *J. Geophys. Res.,* **101,** 12 791–12 794.
Chandrasekhar, S., 1950: *Radiative Transfer*. Clarendon, 393 pp.
Chepfer, H., G. B. Brogniez, P. Goloub, F. M. Breon, and P. H. Flamant, 1999: Observations of horizontally oriented ice crystals in cirrus clouds with POLDER-1/ADEOS-1. *J. Quant. Spectrosc. Radiat. Transfer,* **63,** 521–543.
Cubasch, U., and Coauthors, 2001: Projection of future climate change. *Climate Change 2001: The Scientific Basis, Contribution of Working Group I to the Third Assessment Report of the Intergovernmental Panel on Climate Change*, J. T. Houghton et al., Eds., Cambridge University Press, 527–582.
DAO, cited 1996: Algorithm Theoretical Basis Document for Goddard Earth Observing System Data Assimilation System (GEOS DAS) with a focus on version 2. [Available online at http://gmao.gsfc.nasa.gov/systems/geos4/.]
Fu, Q., and K.-N. Liou, 1993: Parameterization of the radiative properties of cirrus clouds. *J. Atmos. Sci.,* **50,** 2008–2025.
Geier, E. B., R. N. Green, D. P. Kratz, P. Minnis, W. F. Miller, S. K. Nolan, and C. B. Franklin, cited 2001: Single satellite footprint TOA/surface fluxes and clouds (SSF) collection document. [Available online at http://asd-www.larc.nasa.gov/ceres/collect_guide/SSF-CG.pdf.]
Goodberlet, M., C. Swift, and J. Wilkerson, 1990: Ocean surface wind speed measurements of Special Sensor Microwave/Imager (SSM/I). *IEEE Geosci. Remote Sens.,* **GE-28,** 828–832.
Hapke, B., 1986: Bidirectional reflectance spectroscopy, 4, The extinction coefficient and the opposition effect. *Icarus,* **67,** 264–280.
Hess, M., P. Koepke, and I. Schult, 1998: Optical properties of aerosols and clouds: The software package OPAC. *Bull. Amer. Meteor. Soc.,* **79,** 831–844.
Ignatov, A., and L. L. Stowe, 2002: Aerosol retrievals from individual AVHRR channels. Part I: Retrieval algorithm and transition from Dave to 6S radiative transfer model. *J. Atmos. Sci.,* **59,** 313–334.
Kato, S., and N. G. Loeb, 2005: Top-of-atmosphere shortwave broadband observed radiance and estimated irradiance from Clouds and the Earth's Radiant Energy System (CERES) instruments on *Terra* over polar regions. *J. Geophys. Res.,* in press.
Kummerow, C., W. Barnes, T. Kozu, J. Shiue, and J. Simpson, 1998: The Tropical Rainfall Measuring Mission (*TRMM*) sensor package. *J. Atmos. Oceanic Technol.,* **15,** 809–817.
Loeb, N. G., K. J. Priestley, D. P. Kratz, E. B. Geier, R. N. Green, B. A. Wielicki, P. O'R. Hinton, and S. K. Nolan, 2001: Determination of unfiltered radiances from the Clouds and the Earth's Radiant Energy System (CERES) instrument. *J. Appl. Meteor.,* **40,** 822–835.
——, S. Kato, and B. A. Wielicki, 2002: Defining top-of-atmosphere flux reference level for Earth radiation budget studies. *J. Climate,* **15,** 3301–3309.
——, N. M. Smith, S. Kato, W. F. Miller, S. K. Gupta, P. Minnis, and B. A. Wielicki, 2003a: Angular distribution models for top-of-atmosphere radiative flux estimation from the Clouds and the Earth's Radiant Energy System instrument on the Tropical Rainfall Measuring Mission Satellite. Part I: Methodology. *J. Appl. Meteor.,* **42,** 240–265.
——, K. Loukachine, N. M. Smith, B. A. Wielicki, and D. F. Young, 2003b: Angular distribution models for top-of-atmosphere radiative flux estimation from the Clouds and the Earth's Radiant Energy System instrument on the Tropical Rainfall Measuring Mission Satellite. Part II: Validation. *J. Appl. Meteor.,* **42**, 1748–1769.
Loukachine, K., and N. G. Loeb, 2003: Application of an artificial neural network simulation for top-of-atmosphere radiative flux estimation from CERES. *J. Atmos. Oceanic Technol.,* **20,** 1749–1757.
——, and ——, 2004: Top-of-atmosphere flux retrievals from CERES using artificial neural networks. *J. Remote Sens. Environ.,* **93,** 381–390.
Loveland, T. R., and A. S. Belward, 1997: The International Geosphere Biosphere Programme Data and Information System Global Land Cover dataset (DISCover). *Acta Astronaut.,* **41,** 681–689.
Minnis, P., and M. M. Khaiyer, 2000: Anisotropy of land surface skin temperature derived from satellite data. *J. Appl. Meteor.,* **39,** 1117–1129.
——, D. P. Garber, D. F. Young, R. F. Arduini, and Y. Tokano, 1998: Parameterizations of reflectance and effective emittance for satellite remote sensing of cloud properties. *J. Atmos. Sci.,* **55,** 3313–3339.
——, D. F. Young, S. Sun-Mack, P. W. Heck, D. R. Doelling, and Q. Trepte, 2003: CERES Cloud Property Retrievals from Imagers on *TRMM*, Terra, and *Aqua*. *Proc. SPIE 10th Int. Symp. on Remote Sensing: Conf. on Remote Sensing of Clouds and the Atmosphere VII*, Barcelona, Spain, 37–48.
——, A. V. Gambheer, and D. R. Doelling, 2004: Azimuthal anisotropy of longwave and infrared window radiances from CERES *TRMM* and *Terra* data. *J. Geophys. Res.,* **109,** D08202, doi:10.1029/2003JD004471.
Nakajima, T., and M. Tanaka, 1986: Matrix formulations for the transfer of solar radiation in a plane-parallel scattering atmosphere. *J. Quant. Spectrosc. Radiat. Transfer,* **35,** 13–21.
——, and ——, 1988: Algorithms for radiative intensity calculations in moderately thick atmospheres using a truncation approximation. *J. Quant. Spectrosc. Radiat. Transfer,* **40,** 51–69.
Rahman, H., M. M. Verstraete, and B. Pinty, 1993: Coupled surface-atmosphere reflectance (CSAR) model 1. Model description and inversion on synthetic data. *J. Geophys. Res.,* **98,** 20 779–20 789.
Remer, L. A., and Coauthors, 2005: The MODIS aerosol algorithm, products, and validation. *J. Atmos. Sci.,* **62,** 947–973.
Smith, G. L., 1994: Effects of time response on the point spread function of a scanning radiometer. *Appl. Opt.,* **33,** 7031–7037.
——, R. N. Green, E. Raschke, L. M. Avis, J. T. Suttles, B. A. Wielicki, and R. Davies, 1986: Inversion methods for satellite studies of the earth radiation budget: Development of algorithms for the ERBE mission. *Rev. Geophys.,* **24,** 407–421.
Suttles, J. T., B. A. Wielicki, and S. Vemury, 1992: Top-of-atmosphere radiative fluxes: Validation of ERBE scanner inversion algorithm using *Nimbus-7* ERB data. *J. Appl. Meteor.,* **31,** 784–796.
Thomas, G. E., and K. Stamnes, 1999: *Radiative Transfer in the Atmosphere and Ocean*. Cambridge University Press, 517 pp.
Wielicki, B. A., B. R. Barkstrom, E. F. Harrison, R. B. Lee III, G. L. Smith, and J. E. Cooper, 1996: Clouds and the Earth's Radiant Energy System (CERES): An Earth observing system experiment. *Bull. Amer. Meteor. Soc,* **77,** 853–868.
Wilber, A. C., D. P. Kratz, and S. K. Gupta, 1999: Surface emissivity maps for use in satellite retrievals of longwave radiation. NASA Tech. Rep. TP-1999-209362, 35 pp.
Young, D. F., P. Minnis, D. R. Doelling, G. G. Gibson, and T. Wong, 1998: Temporal interpolation methods for the Clouds and the Earth's Radiant Energy System (CERES) experiment. *J. Appl. Meteor.,* **37,** 572–590.